Article:
Scott, L, Borissova, A, Burns, A et al. (1 more author) (2021) Effect of grinding nozzles pressure on particle and fluid flow patterns in a spiral jet mill. Powder Technology, 394. pp. 439-447. ISSN 0032-5910

https://doi.org/10.1016/j.powtec.2021.07.090

EFFECT OF GRINDING NOZZLES PRESSURE ON PARTICLE AND FLUID FLOW PATTERNS IN A SPIRAL JET MILL

Lewis Scott, Antonia Borissova, Alan Burns and Mojtaba Ghadiri*

School of Chemical and Process Engineering, University of Leeds, Leeds LS2 9JT, UK

*Corresponding author: M.Ghadiri@leeds.ac.uk

Abstract

Spiral jet mills utilise high-pressure gas jets, which induce particle breakage by collisions. Appropriately angled jets force particles to circulate in dense phase near the wall due to the centrifugal field. Moving radially inwards towards the mill centre, the two-phase dense flow is transformed into a lean phase and fine particles are entrained out by the fluid drag. Here we analyse the effect of grinding nozzles pressure on the particle dynamics and fluid flow by numerical simulation. The average velocity gradient in the radial direction is very steep for low mass loadings, indicative of rapid shearing, but it decreases significantly as the particle mass loading is increased. The dissipated collisional energy, accountable for size reduction, is strongly influenced by the jet penetration through the circulating bed, which in turn depends on the mass loading and operating pressure of grinding gas nozzles. As a result of jet penetration, the grinding gas nozzles pressure becomes less effective at high pressures. The analysis developed here elucidates the coupled effect of mass loading and grinding nozzles pressure on the dissipated collisional energy, which accounts for particle breakage.

Keywords: spiral jet mill, grinding gas pressure, fluid flow pattern, particle dynamics, collisional energy, jet penetration, simulation, CFD-DEM

Introduction

Mechanistically simple in its design, the spiral jet mill is the equipment of choice for many industries that process fine powders. The mill has no moving parts, as it is operated using high pressure gas through nozzles, providing fluid energy for grinding and milling. This leads to low maintenance effort and contamination of the final product. The grinding gas nozzles induce an internal vortex and cause interparticle collisions. Once the material has been sufficiently reduced in size, the drag force of the grinding fluid overcomes the centrifugal force acting on the particles and entrains them out of the mill through a central port. Due to both breakage and classification occurring simultaneously within the milling chamber, subtle changes in either the particle or gas feed rates during operation can alter the flow behaviour within the milling chamber and change the final product size.

During operation, a bed of particles forms along the outer wall of the milling chamber under the centrifugal action that is induced by the grinding gas jets. The bed circulates in the chamber and the particle layers along the bed depth shear against each other. It has been shown experimentally by Luczak et al. [1] using particle velocimetry, and through coupled Computational Fluid Dynamics – Discrete Element Method (CFD-DEM) simulations by Scott et al. [2] that near the bed surface the particle velocity has a steep gradient causing rapid shear straining, whilst particle layers closest to the wall travel slowly and are exposed to less shearing. Particles are also subjected to high velocity collisions as they are ejected from the bed by the gas jets and also upon collision with the bed surface further downstream [3]. Therefore, inside the mill particle size reduction is induced, where high shear straining and collisions prevail near the bed surface, rather than within the bed [4].

As the pressure of the grinding gas is increased, the fluid energy available for breakage also increases. The particles experience greater acceleration and are subjected to high impact velocities. This could produce finer products at higher pressures [5–7], although the decrease

50 in product size is not linearly proportional to the increase in pressure [8–9]. Surface flaws in a
51 material leads to the initial size reduction. However, as particle size decreases, their collision
52 energy also decreases, thereby reducing the extent of breakage [10]. Using a coupled CFD-
53 DEM simulation approach, Brosh et al. [11] found that when the grinding gas pressure was
54 decreased the size distribution of the particles leaving the mill widened. Similarly, Muller et
55 al. [12] found that decreasing the grinding gas pressure significantly leads to vortex instability
56 and poor classification. They considered 8 barg pressure to be acceptable for the operation of
57 their mill and solid feed rate used. They reduced the pressure to 4 barg and the result was a
58 poor classification, widening the product size distribution due to vortex instability, which they
59 monitored using piezoelectric pressure sensors. After reducing the injector nozzles pressure to
60 2 barg, they noted that the material travelled directly from the injector to the vortex finder.
61 Both Rodnianski et al. [13] and Bnà et al. [14] analysed the fluid flow field as a function of
62 pressure. They showed that as the grinding pressure was increased the ratio of the tangential
63 and radial gas velocity components v_t/v_r remained constant.. However, in Rodnianski et al. [13]
64 study, only CFD simulations were used to analyse the flow field, ignoring particle fluid
65 interactions and Bnà et al. [14] used a one-way coupled CFD-DEM apporach. Unlike two-way
66 or higher-order coupling schemes, CFD only and one-way coupling systems cannot capture the
67 dampening affect of particles on the fluid flow field in such dense systems.

68 The pressure at which the grinding gas is supplied to the mill determines the vortex
69 stability and the fineness of the product. Using a four-way coupled CFD-DEM approach [15–
70 18] here, the fluid flow field, particle velocity distribution and particle collision intensity are
71 analysed as a function of the grinding gas nozzles pressure and mass loading. The focus of the
72 study is to understand how the grinding gas pressure affects the fluid flow field and particle
73 bed dynamics during operation. So, particle breakage is not addressed.

Methodology

The mill used for simulation is based on the design of the Hosokawa Micron AS-50 spiral jet mill, whilst using an in-house drawing made at the University of Leeds, as shown in Figure 1. The main milling chamber is 50 mm in diameter and highlighted in red. The gas/air injector nozzle (a) acts as a Venturi eductor, entraining the feed particles from the funnel and and injecting them at the top of the milling chamber, somewhere at the mid radial position in the chamber (*NB* in this work the particles are directly placed in the milling chamber to save simulation time). The pipe (b) feeds pressurised air into an annular manifold, which in turns feeds the four grinding nozzles (c). The nozzles are equally spaced and angled at 40° with respect to the outer wall tangent. The manifold has been included in the simulation, as it was found by Dogbe [4] to alter the flow field within the grinding chamber when it was not present. A special design feature of the AS-50 mill is the central classifier section. The gas is forced up by the classifier (d) in a narrow passage almost vertically into a hemispherical chamber before it is directed downwards by the vortex finder (e) and out of the mill and into a catch pot (f). As mentioned above, in these simulations, no particles are introduced through the hopper section (g). Nevertheless, the section has been included as it is important to account for the gas through the injector nozzle and also the induced air from the feed funnel into the mill.

In total five grinding nozzles pressure settings were investigated (2, 3, 4, 5 and 6 barg) along with the six mass loadings (0.4, 0.8, 1.2, 1.6, 2.0 and 2.4 g), for which the associated particle number of each case is detailed in Table 1. The total time for each simulation was 0.1 s. For each mass loading, the addition rate of particles was set so that all particles were added by 0.01 s directly into the chamber in an annular region, using the standard EDEM^{TM} particle generating factory. The annular region was bounded by the wall and a radial position 7.5 mm from the wall. Placing the factory inside the mill chamber decreased the total simulation time. Spherical particles with a base radius, r, of 100 µm and a random distribution of (0.8-1.2)×r

were used. The particle bed was then allowed time to form and reach a pseudo steady-state before any results were recorded. The time needed for the particles to achieve this state typically took around 0.02 s. However, a further 0.04 s was allowed before any time-sensitive data were collected.

Figure 1: An in-house made CAD drawing of Hosokawa Micron AS-50 mill.

The particle motion was calculated using EDEM^{TM} 2019 (Altair, UK) and the fluid flow field was resolved by ANSYS Fluent 18.1. A four-way coupling scheme was adopted to capture the fluid-particle interactions in this study. The spherical drag model by Morsi and Alexander [19], along with the k-ε-RNG turbulence model with scalable wall functions and the 'SIMPLE' pressure-velocity coupling scheme for the spatial discretisation were used in Fluent 18.1. The mesh size was based on the largest particle size (240 μm) and a maximum particle-to-fluid cell volume ratio of 40% was selected, as recommended by Norouzi et al. [18]. The particle parameters such as the coefficient of restitution and friction are listed in Table 2, along with the time steps used for both the fluid and particle systems. A ratio of 20 particle time steps to 1 fluid time step was adopted, as also recommended by Norouzi et al. [18]. The fluid flow field was first resolved before the particles were added.

Table 1: Fluid pressure settings and mass loadings

Table 2: Fluid and particle properties and parameters used in the simulation

Results

The average particle velocity magnitude for each combination of mass loading and pressure is shown in Figure 2 as a function of the radial position from the chamber wall. The

data are collected from a slice $8d_p$ deep in the circumferential direction at a position that is equidistant between two nozzles, as shown in Figure 3. The data acquisition is over 300 time steps and is limited to a distance up to 12 mm from the wall, as few particles travel radially inward past this point. To reduce the noise in the data caused by fluctuations in the particle velocity, a moving average approach is used. A maximum of 30 data points are chosen for averaging when plotting the data from the wall to the bed surface.

Considering the pressure range analysed, the 2 barg and 6 barg cases have the lowest and highest profiles, respectively, of the average particle velocity magnitude for all the pressures investigated, as intuitively expected. The particles associated with the lowest mass loading, i.e. 0.4 g case (blue), have the highest profile of the average particle velocity magnitude, due to the small number of particles accelerated by the fluid. In this case the largest particle velocity magnitude is around 13 m/s. As the mass loading is increased, the magnitude of the particle velocity decreases. Interestingly, its gradient within the dense bed region also decreases, as indicated by the slopes of the profiles. The bed moves more like a 'plug' near the wall for large mass loadings, as the velocity gradient is very small. Beyond 10 mm towards the centre, the particles are in a lean phase form and the profiles are unreliable as a small number of particles are present.

Increasing the nozzles pressure to 3 barg increases the particle velocity magnitude. The profiles depict the same overall trend as the case of 2 barg, with the 0.4 g case displaying the largest particle velocity and the 2.0 g and 2.4 g cases showing the smallest and also overlapping. As the mass loading is increased, the low velocity region near the wall grows and extends further towards the centre of the mill. The bed surface in all cases is rapidly shearing as indicated by the high velocity gradient.

146 The particle velocity distributions seen in the 4, 5 and 6 barg cases follow the same
147 trend as the 3 barg case. An increase in the grinding nozzles pressure leads to an overall increase
148 of the corresponding velocity at a given radial position. Moreover, as the pressure is increased,
149 the velocity distributions shift notably to the right, indicating a change in the bed dynamics.
150 As the mass loading is increased, particularly in the cases of 1.6, 2.0 and 2.4 g loadings, the
151 very low velocity gradient close to the wall is indicative of lack of extensive shear straining in
152 the circulating bed. Such a situation does not have potential to contribute significantly to
153 particle milling. The velocity profiles of 2.0 and 2.4 g loadings overlap close to the wall and
154 indicate a 'saturation' state for the particle hold-up.

155

156 *Figure 2: Profile of particle velocity magnitude as a function of distance from the outer wall for different holdup loadings*
157 *and pressures.*

158

159 *Figure 3: Construction slice used to produce particle velocity magnitude plot. Slice constructed at 45° (blue) from the nozzle*
160 *(N1) with a thickness of 8 particle diameters.*

161

162 The 'heat maps' of fluid velocity have been plotted in Figure 4. They show a view of
163 the mid-plane for each resulting fluid flow field for 1.2 g of material hold-up as an example.
164 As the nozzles pressure is increased the fluid velocity magnitude also increases, as would be
165 expected. However, when examining the area that is occupied by the particle bed, the fluid
166 velocity there is low with little variations even for the high grinding nozzles pressures, such as
167 6 barg. This is because the jets penetrate through the bed and do not transfer much of their
168 energy to the particles. In the 2 barg and 3 barg cases, the jets dissipate before reaching the lean
169 phase section of the milling chamber and appear as submerged. In contrast, in the 4, 5 and 6
170 barg cases, the pressure is sufficiently high that the jets penetrate through the bed and eject
171 their momentum into the lean phase. This reduces the total energy transferred from the fluid

172 to the circulating bed. Consequently, the particles closest to the wall experience little change
173 in velocity as the grinding nozzles pressure is increased .

174

175 *Figure 4: Heat map of the fluid flow field velocity magnitude for the 1.2 g loadings at different nozzles pressures.*

176 Once the jet has penetrated through the bed, a forced vortex prevails, followed by a free
177 vortex in the classifier region. The pressure heat map is shown in **Error! Reference source**
178 **not found.**, depicting the pressure field of the 1.2 g case at 5 barg as an example. The pressure
179 scale colour bar is in gauge pressure and the upper limit has been clipped to 10 kPa to highlight
180 the gradient inside the milling chamber. This limit was placed as the pressure gradient could
181 not be viewed due to high pressure at the nozzles. In Figure 5, the left figure shows the pressure
182 field on a z-plane at mid-height position in the chamber, whilst the right figure shows its profile
183 on a plane encompassing the z-axis and the two opposing jets at their mid plane at 90° angle
184 from the x-axis. It can be seen the pressure in the milling chamber is only marginally (7 kPa)
185 above the atmospheric pressure, and with little gradient across the chamber. Since the jets
186 penetrate through the bed for the high-pressure cases (i.e. 4 barg and greater), the potential to
187 exchange energy with the particles in the bed is limited at this mass loading. There is a large
188 pressure drop in the classifier zone. The flow is accelerated in this zone, due to the constriction,
189 but the pressure drop is not recovered, and the air flows up over the classifier ring and proceeds
190 to exit the mill to atmospheric pressure.

191

192 *Figure 5: Fluid pressure field for the 5 barg case with 1.2 g of mass loading. Mid-plane view (left) and x-plane view (right).*
193

194 To assess how the entire particle system is affected by the increase in the gas pressure
195 at the grinding nozzles, the total instantaneous kinetic energy of all the particles has been

plotted for each combination of mass loading and pressure in *Figure 6*. Each plot depicts the simulations from time t = 0.0 s to t = 0.1 s. There is a sharp increase in the kinetic energy at the beginning of each profile. This is because the particles are released at zero velocity in the mill over the time interval up to 0.01 s (with the fluid flow already fully resolved) and are accelerated by the fluid power. There is a noticeable peak during the acceleration phase for high mass loadings. This is due to the random positioning of the particles when added to the mill within the factory area. The particles are well-spaced from each other and the fluid flow field is not dampened at the time of particle loading, giving rise to effective uptake of fluid energy by the particles. Once the particles form a circulating bed along the outer wall, they travel in a region of dampened fluid and their kinetic energy approaches an asymptotic value.

Starting with the 2 barg case, there are some initial variations in the kinetic energy amongst the mass loadings, but they all reach a single asymptotic value at long times. The same also roughly holds for all mass loadings in the 3 barg case. This is highly remarkable, as irrespective of the mass loading, the particle system reaches the same asymptotic level for the given nozzles pressure. At low nozzles pressures the particles kinetic energy varies inversely with mass loading. This trend is related to the grinding nozzles jet being submerged in the circulating bed. At higher pressures, i.e., in the 4, 5 and 6 barg cases, there is some disparity in the kinetic energy of the particle system, accompanied by fluctuations, as the mass loading is increased. The difference in the trends between the low (2 and 3 barg) and high (4-6 barg) pressure cases suggests a change in the particle dynamics due to jet penetration. For the low-pressure cases, the jets are submerged in the bed, and therefore, a higher fraction of the fluid input energy is exchanged with the particles before the air passes into the lean phase section of the mill. In contrast, in the high-pressure cases, the jets penetrate through the bed and therefore a smaller fraction of the input energy is exchanged with the bed particles. Consequently, the asymptotic value of the kinetic energy decreases as the mass loading is increased up to 1.6 g

(albeit with fluctuations). Beyond this mass loading, the trend reverses as the jets can no longer penetrate through the moving bed into the lean phase, and hence the energy is transferred more readily into the bed. This can be viewed most clearly in the 6 barg case. The kinetic energy decreases as the mass is increased from 0.4 g to 1.6 g, and then increases at 2.0 g and again at 2.4 g. Nonetheless, in the simulations here, the kinetic energy of the system increases roughly proportionally from 5 mJ to 14 mJ, as the pressure is increased from 2 to 6 bar for the 1.2 g case. However, it is the collisional energy rather than the total kinetic energy of the particles in the mill that is accountable for size reduction. The change in the jet penetration trend from the submerged mode to the case of penetrating the moving bed undoubtedly influences the overall energy utilised by the particle system.

The dissipated collisional energy is shown in Figure 7 for the mass loading of 1.2 g as an example. This is calculated as the difference between the incident and rebound kinetic energy of each particle summed up over the total number of particles. Interestingly, there is little increase in the dissipated energy as the pressure is increased from 5 to 6 barg. This is in line with observations of Ramanujam and Venkateswarlu [8] and Kürten & Rumpf [9], who noted that increasing the pressure does not lead to a proportional decrease in product size, as in fact, the fluid energy is under-utilised by the particle system.

Figure 6: Kinetic energy of the particle system for each combination of mass loading and pressure.

Figure 7: Total instantaneous dissipated kinetic energy through collisions from time 0.07 s to 0.1 s for the 1.2 g mass loading

A spatial map of the dissipated energy is shown in Figure 8: Cumulative dissipated energy recorded over 0.03 s for the 1.2 g mass loading for each pressure case

246 , based on the data of Figure 7. Each spatial map depicts the cumulative dissipated
247 energy over the final 0.03 s of the simulation. The high velocity particles expelled by the jets
248 create a square boundary around the outer region of the lean phase. The shape is due to the fact
249 that no particle is capable of reaching the classifier ring due to their size, as their own inertia
250 carries them back to the chamber wall. The shape of the lean region is also not symmetrical,
251 due to the position of the feed pipe, providing additional air into the mill at high fluid velocity.
252 Interestingly, although the pressure is increased from 2 to 6 barg, there are areas of the bed that
253 show almost no change in the dissipated energy. This observation further advocates the idea
254 that the mechanical energy exchange of the fluid (air in this case) with the particles becomes
255 more limited as the pressure is increased. Areas where the particles come into direct contact
256 with the high-velocity fluid field, i.e. in front of the injector gas nozzles or along the bed face,
257 show an increase in energy transfer. However, areas close to the wall and inside the bed, show
258 little increase in the energy transfer because the air bypasses the bed through jet penetration.

259

260

261 *Figure 8: Cumulative dissipated energy recorded over 0.03 s for the 1.2 g mass loading for each pressure case*

262

263

264 To explore the dependence of the accumulated particle kinetic energy and dissipated energy,
265 as determined above, on the grinding fluid power (*W*), the latter is calculated from the pressure
266 drop across each nozzle and the mass flux, given by equation (1) by Tilton [20].

267 $$G = P_o \sqrt{\frac{\gamma M_w}{RT_o}} \frac{M_1}{(1+\frac{\gamma-1}{2}M_1^2)^{(\gamma+1)/2(\gamma-1)}} \quad (1)$$

where G is the mass flux, P_o and T_o are the upstream pressure and temperature, respectively. M_w is the molecular weight of the gas, R is the gas constant, M_1 is the Mach number and γ is the ratio of the specific heat capacities at constant pressure and constant volume. The results are given in Figures 9 and 10 for the kinetic energy and dissipated energy, respectively. As the mass loading is increased from 0.4 g to 1.6 g, the kinetic energy of the system first decreases, and then it increases for higher loadings. This is because the jets are no longer able to penetrate through the bed, thus resulting in a change in particle dynamics.

Figure 9: Average particle system kinetic energy (mJ) for each mass loading as a function of the calculated grinding nozzle fluid power (W)

The dissipated energy per particle for the entire simulation time for the two cases of 1.2 g and 2.4 g is shown as a function of grinding fluid power in Figure 10. The particles in the 1.2 g loading case consistently dissipate more energy through collisions than in the 2.4 g case, even though they have the same system kinetic energy, as shown in Figure 9. Once again, the particle dynamics within the mill changes once the jets become submerged. The sudden change in the trend in the 1.2 g case is for the same reason as can be seen in Figure 7, i.e., the jets are penetrating the bed and the fluid leaving the mill without transferring energy to the particles.

Figure 10: Average particle dissipated kinetic energy (mJ) lost through particle collisions as a function of the calculated power supplied by the grinding jets (W)

Conclusions

Using a four-way coupled DEM-CFD simulation methodology, the particle dynamics and fluid motion in a spiral jet mill (Hosokawa Micron AS-50) were analysed for four grinding gas nozzles pressure cases (2, 3, 4, 5 and 6 barg) and six mass loadings of 0.4, 0.8, 1.2, 1.6, 2.0 and 2.4 g. In each pressure case, the mass loading was varied and the patterns of particle dynamics and fluid flow were analysed. It is shown that the average particle velocity increases as the pressure of the grinding gas nozzles is increased. However, at large mass loadings of 1.6,

2.0 and 2.4 g, the particles nearest the wall are not affected much by the pressure increase and their velocity gradient is small. There is a large decrease in the average particle velocity at high mass loadings, as the jets become submerged. In this case, the particles are not ejected at high velocity into the lean phase of the milling chamber.

The dissipated collisional energy, accountable for size reduction, is strongly influenced by the particle dynamics associated with the jet penetration. Depending on the mass loading and operating gas nozzles pressure, the jets can penetrate through the moving bed. In this situation rapid shearing occurs near the bed surface and particles experience high velocity collisions, promoting milling. When the jets are submerged, shearing is reduced and the average particle velocity decreases. This change in the particles dynamics leads to a decrease in the dissipated energy, despite the kinetic energy remaining constant.

Acknowledgements

This project is supported by the Engineering and Physical Sciences Research Council, UK, through the Centre of Doctoral Training for Complex Particulate Products and Processes (CDT CP^3) (EPSRC Grant EP/L015285/1), which forms a part of the doctoral studies in collaboration with AstraZeneca Ltd. The authors gratefully acknowledge their support and would also like to especially thank Ian Gabbott and Catherine Hallam for their project co-ordination. We are also thankful to DEM Solutions (now Altair), Edinburgh, UK, for providing a special license for the EDEM software for use in this work.

References

1. B. Luczak, R. Müller, C. Kessel, M. Ulbricht, & H. J. Schultz, Visualization of flow conditions inside spiral jet mills with different nozzle numbers– Analysis of unloaded and loaded mills and correlation with grinding performance. *Powder Technology*, **342** (2019) 108–117. https://doi.org/10.1016/j.powtec.2018.09.078.

2. L. Scott, A. Borissova, A. Burns, & M. Ghadiri, Influence of holdup on gas and particle flow patterns in

a spiral jet mill. *Powder Technology*, **377** (2021) 233–243. https://doi.org/10.1016/j.powtec.2020.08.099.

3. S. Bhonsale, L. Scott, M. Ghadiri, & J. Van Impe, Numerical Simulation of Particle Dynamics in a Spiral Jet Mill via Coupled CFD-DEM. *Pharmaceutics*, **13** (2021) 937. https://doi.org/10.3390/pharmaceutics13070937.

4. S. C. Dogbe, Predictive Milling of Active Pharmaceutical Ingredients and Excipients, The University of Leeds, 2017.

5. R. Tuunila & L. Nyström, Effects of grinding parameters on product fineness in jet mill grinding. *Minerals Engineering*, **11** (1998) 1089–1094. https://doi.org/10.1016/S0892-6875(98)00095-8.

6. A. Katz & H. Kalman, Preliminary experimental analysis of a spiral jet mill performance. *Particle and Particle Systems Characterization*, **24** (2007) 332–338. https://doi.org/10.1002/ppsc.200601114.

7. S. Teng, P. Wang, Q. Zhang, & C. Gogos, Analysis of Fluid Energy Mill by gas-solid two-phase flow simulation. *Powder Technology*, **208** (2011) 684–693. https://doi.org/10.1016/j.powtec.2010.12.033.

8. M. Ramanujam & D. Venkateswarlu, Studies in fluid energy grinding. *Powder Technology*, **3** (1969) 92–101. https://doi.org/10.1016/0032-5910(69)80060-4.

9. H. Kürten & H. Rumpf, Zerkleinerungsuntersuchungen mit tribolumineszierenden Stoffen. *Chemie Ingenieur Technik*, **38** (1966) 331–342. https://doi.org/10.1002/cite.330380327.

10. D. Behrens, Prallzerkleinerung von Glas-Kugeln und unregelmäßig geformten Teilchen aus Schwerspat, Kalkstein und Quarzsand. *Chemie Ingenieur Technik*, **37** (1965) 473–483. https://doi.org/10.1002/cite.330370503.

11. T. Brosh, H. Kalman, A. Levy, I. Peyron, & F. Ricard, DEM-CFD simulation of particle comminution in jet-mill. *Powder Technology*, **257** (2014) 104–112. https://doi.org/10.1016/j.powtec.2014.02.043.

12. F. Müller, R. Polke, & G. Schädel, Spiral jet mills: hold up and scale up. *International Journal of Mineral Processing*, **44–45** (1996) 315–326. https://doi.org/10.1016/0301-7516(95)00042-9.

13. V. Rodnianski, N. Krakauer, K. Darwesh, A. Levy, H. Kalman, I. Peyron, & F. Ricard, Aerodynamic classification in a spiral jet mill. *Powder Technology*, **243** (2013) 110–119. https://doi.org/10.1016/j.powtec.2013.03.018.

14. S. Bnà, R. Ponzini, M. Cestari, C. Cavazzoni, C. Cottini, & A. Benassi, Investigation of particle dynamics and classification mechanism in a spiral jet mill through computational fluid dynamics and discrete element methods. *Powder Technology*, **364** (2020) 746–773. https://doi.org/10.1016/j.powtec.2020.02.029.

15. Y. Tsuji, T. Tanaka, & T. Ishida, Lagrangian numerical simulation of plug flow of cohesionless particles in a horizontal pipe. *Powder Technology*, **71** (1992) 239–250. https://doi.org/10.1016/0032-5910(92)88030-L.

16. A. Di Renzo, F. P. Di Maio, R. Girimonte, & B. Formisani, DEM simulation of the mixing equilibrium in fluidized beds of two solids differing in density. *Powder Technology*, **184** (2008) 214–223. https://doi.org/10.1016/j.powtec.2007.11.031.

17. S. Elghobashi, Particle-laden turbulent flows: direct simulation and closure models. In: Oliemans R.V.A. (eds) *Computational Fluid Dynamics for the Petrochemical Process Industry*. Springer, Dordrecht (1991). https://doi.org/10.1007/978-94-011-3632-7_4.

18. H. Norouzi, R. Zarghami, R. Sotudeh-Gharebagh, & N. Mostoufi, *Coupled CFD-DEM Modeling* (Chichester: John Wiley & Sons, 2016).

19. S. A. Morsi & A. J. Alexander, An investigation of particle trajectories in two-phase flow systems. *Journal of Fluid Mechanics*, **55** (1972) 193–208. https://doi.org/10.1017/S0022112072001806.

20. D. W. Green & M. Z. Southard, *Perry's Chemical Engineers' Handbook, 9th Edition* (McGraw-Hill Education, 2019).

366

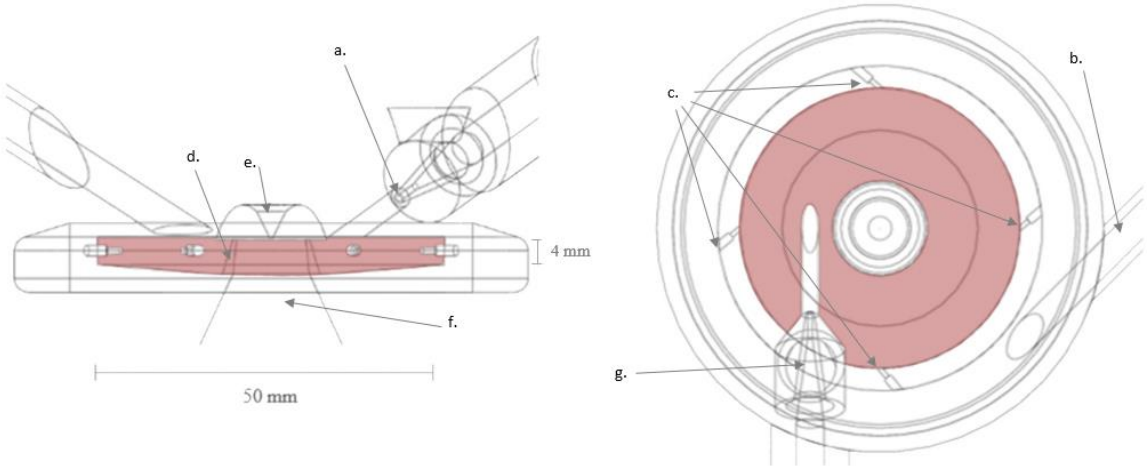

367

368 *Figure 11: An in-house made CAD drawing of Hosokawa Micron AS-50 mill; (a) injector nozzle, (b) grinding air supply, (c)*
369 *grinding nozzles, (d) classifier ring, (e) vortex inductor, (f) mill exit and (g) hopper entrance.*

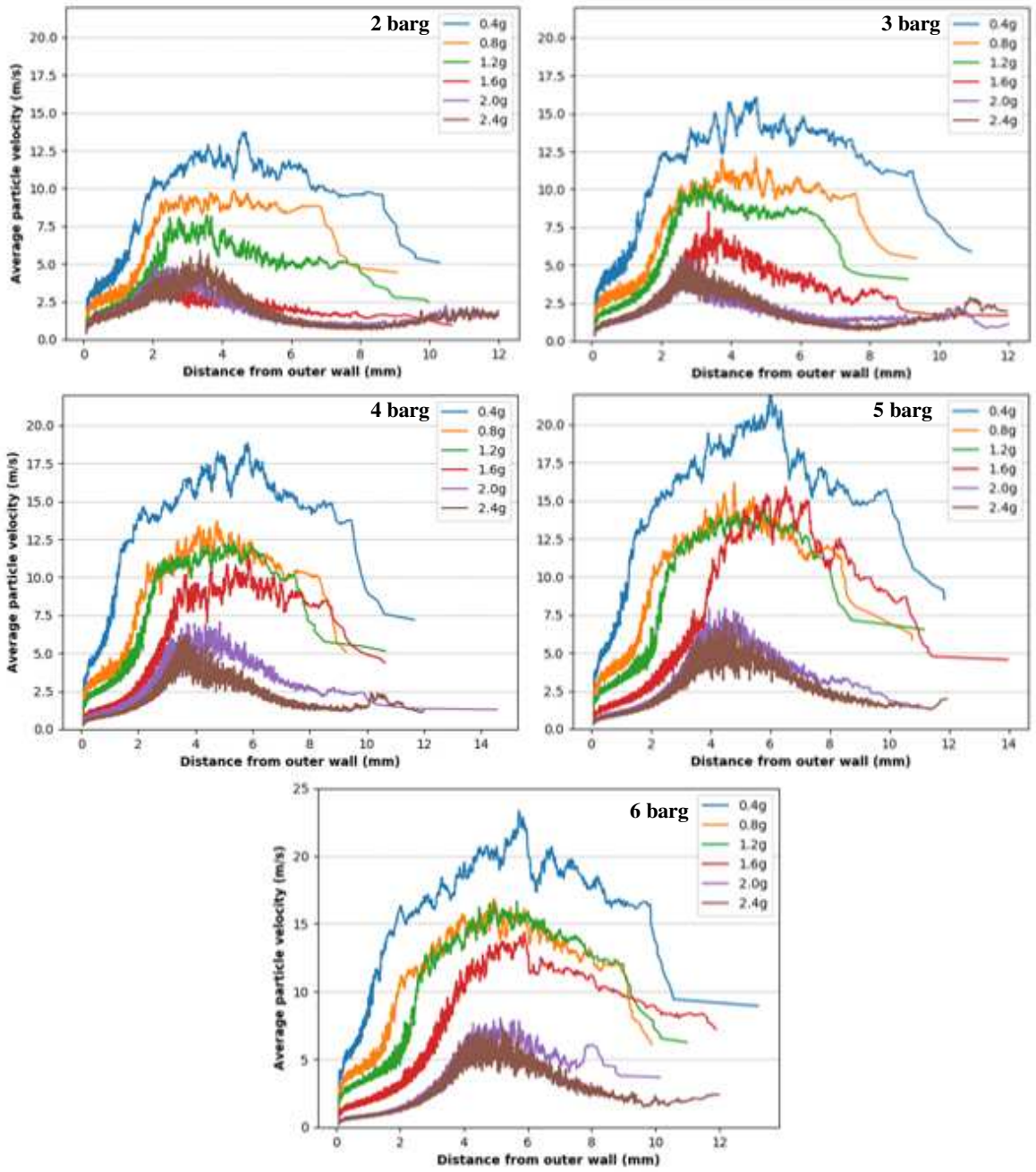

370

371 *Figure 12: Profile of particle velocity magnitude as a function of distance from the outer wall for different holdup loadings*
372 *and pressures.*

373

374

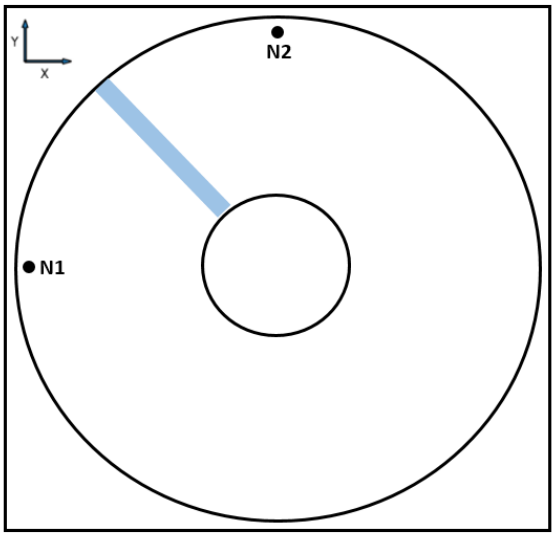

375

376 *Figure 13: Construction slice used to produce particle velocity magnitude plot. Slice constructed at 45° (blue) from the*

377 *nozzle (N1) with a thickness of 8 particle diameters.*

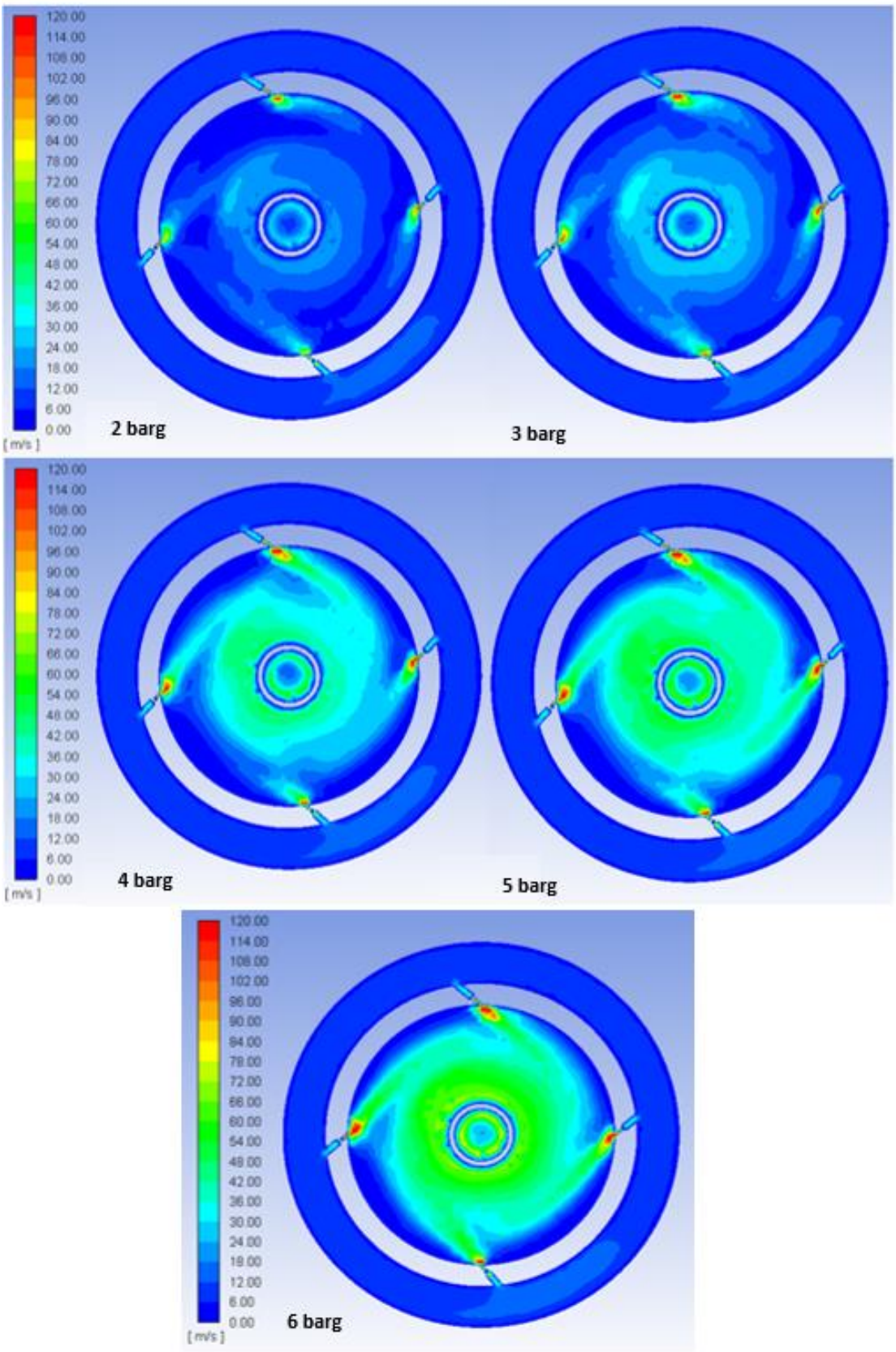

Figure 14: Heat map of fluid flow field velocity magnitude (m/s) ~~plots~~ for the 1.2 g loadings at different given pressures.

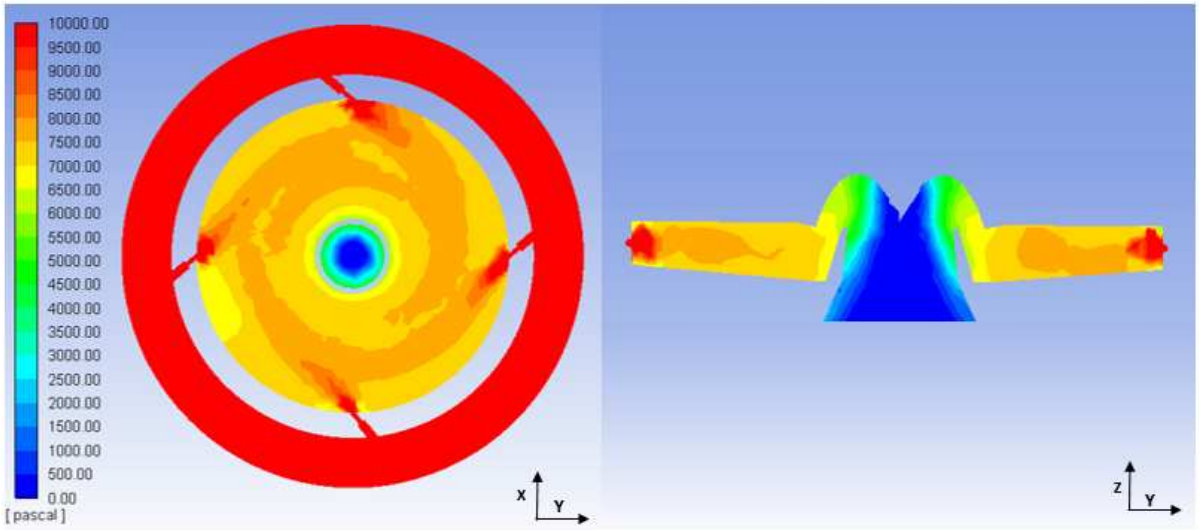

Figure 15: Fluid pressure field for the 5 barg case with 1.2 g mass loading. Mid-plane view (left) and x-plane view (right).

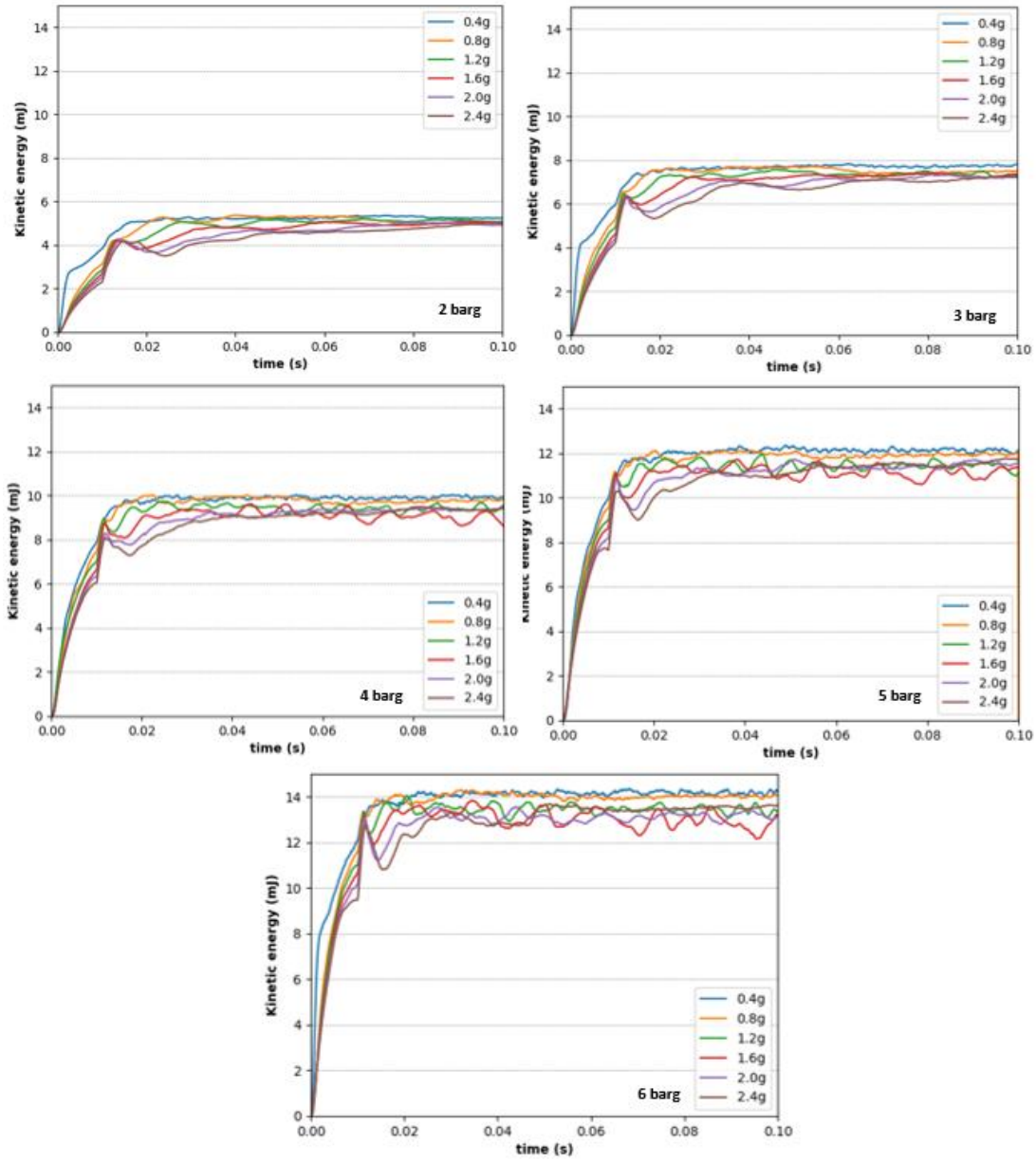

Figure 16: Kinetic energy of the particle system for each combination of mass loading and pressure.

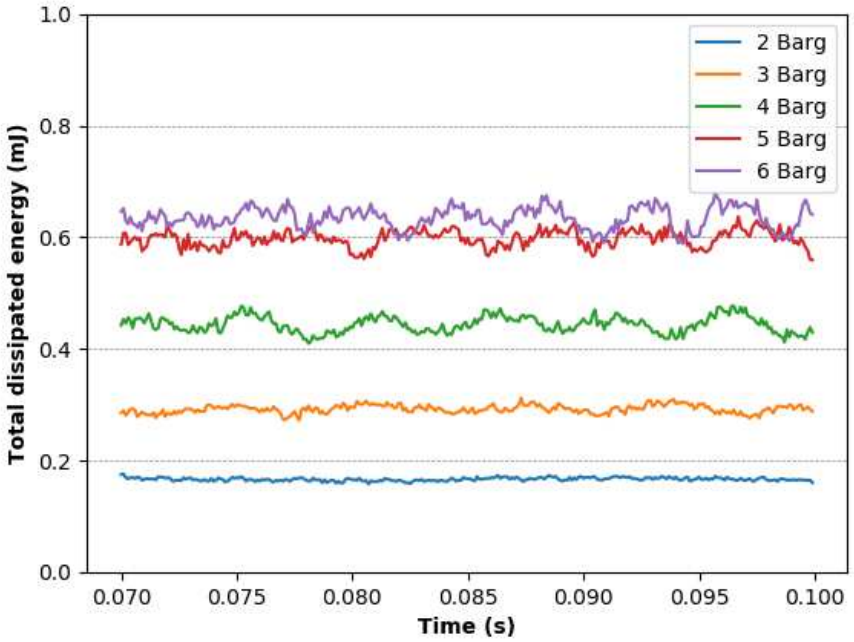

392

393 *Figure 17: Total instantaneous dissipated kinetic energy through collisions from time 0.07 s to 0.1 s for the 1.2 g mass*
394 *loading*

395

396

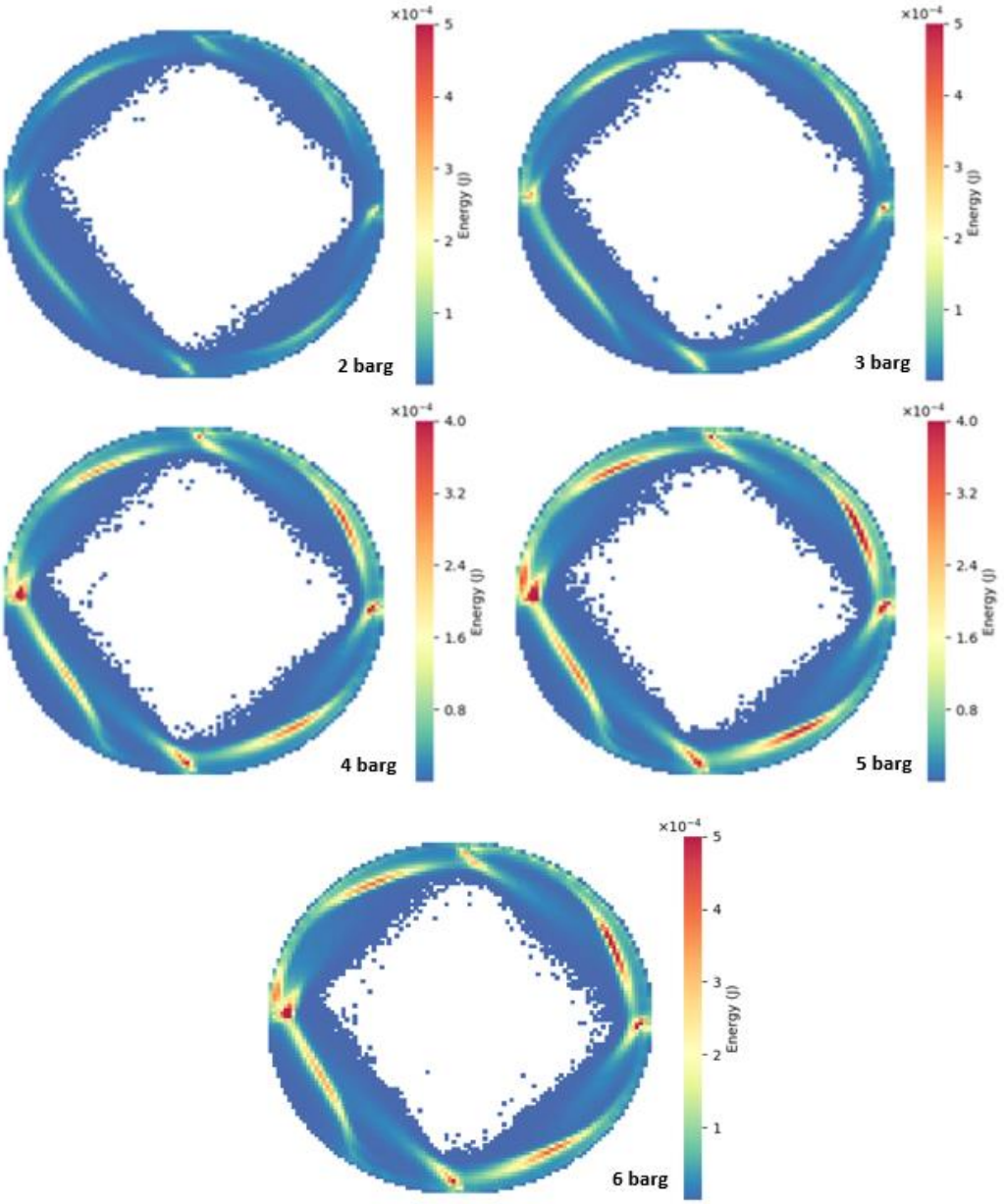

Figure 18: Cumulative dissipated energy recorded over 0.03 s for the 1.2 g mass loading for each pressure case

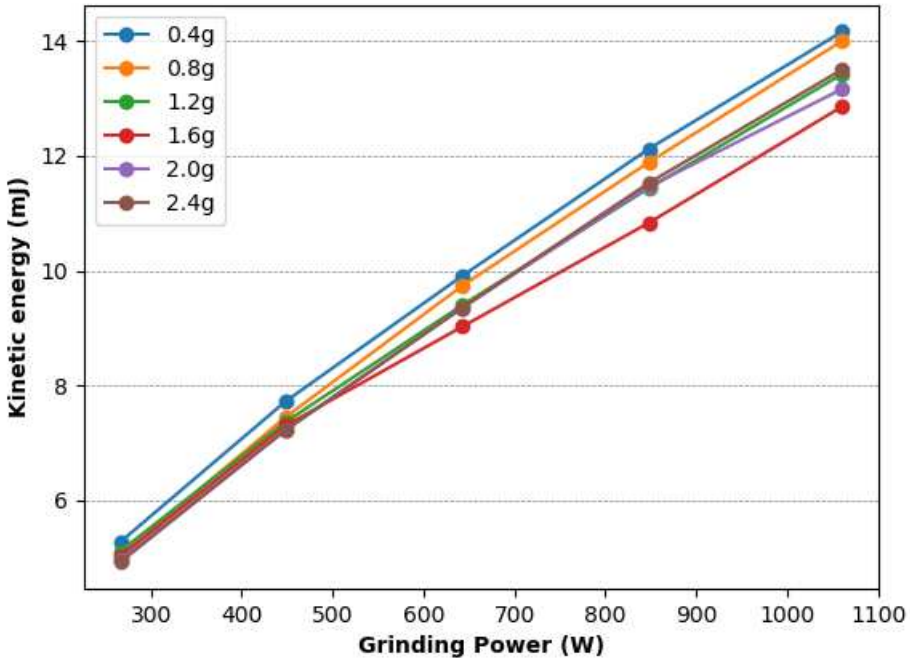

Figure 19: Average particle system kinetic energy (mJ) for each mass loading as a function of the calculated grinding nozzle fluid power (W)

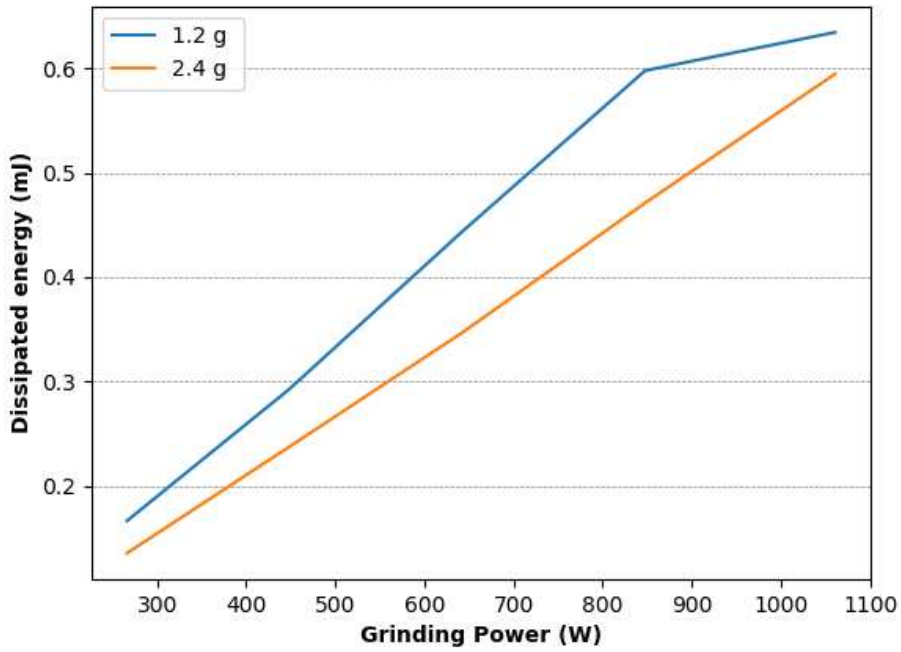

Figure 20: Average particle dissipated kinetic energy (mJ) lost through particle collisions as a function of the calculated power supplied by the grinding jets (W)

407

408 *Table 3: Fluid pressure settings and mass loadings*

Feed Gas Injector Nozzle Pressure (barg)	3	4	5	6	7
Grinding Gas Nozzles Pressure (barg)	2	3	4	5	6
Mass Loading(g)	Particle number				
0.4	61857	61869	61701	61884	61822
0.8	123684	123481	123467	123404	123535
1.2	184576	184958	184796	184763	184596
1.6	246368	246025	246248	245892	245779
2.0	310191	308539	307964	307393	307675
2.4	383380	373565	371522	371471	370853

409

410 *Table 4: Fluid and particle properties and parameters used in the simulation*

Phase	Parameter	Value
Fluid	Viscosity, Pa/s	0.000018
	Fluid time step, µs	8 – 20
	Minimum edge length (particles present), µm	630
	Minimum edge length (no particles present), µm	400
Particle	Radius (µm)	100
	Density, kg/m^3	1500
	Size distribution	0.8-r-1.2
	Shear modulus, MPa	10
	Poisson's ratio	0.25
	Coefficient of restitution	0.5
	Coefficient of static friction	0.5
	Coefficient of rolling friction	0.01
	DEM time step, µs	0.4 – 1.0

411